A Computational Study of the Impact of Fluid Structure Interaction on the Development and Persistence of 2D LEVs in Low Reynolds Number Flow Applications

Antonio Monteiro [*], Katherine M. Vail [†]

University of Massachusetts Lowell, Lowell, MA, 01854, USA.

and Anya Jones [‡]

University of Maryland College Park, College Park, MD, 20742, USA

Per Olof Persson [§]

University of California Berkeley, Berkeley, CA, 94720, USA.

David J. Willis[¶]

University of Massachusetts Lowell, Lowell, MA, 01854, USA.

This paper examines how torsional spring stiffness about a wing's leading edge impacts leading edge vortex (LEV) development and persistence. We use a low fidelity potential flow, 2-D linear strength doublet lattice method to perform exploratory parameter sweeps. In this model, the leading-edge vortex shedding is based on an LESP criterion and trailing edge shedding based on a traditional Kutta condition. Using this low-fidelity tool, we explore a large array of parameter sweeps (spring stiffness, camber, and initial wing angle) to understand how passive leading edge compliance affects LEV development.

For the cases that were examined, leading edge passive structural compliance led to lower lower lift and drag forces and earlier LEV separation from the wing. Positive camber had a slight negative effect on the persistence of the LEV when compared with symmetric and negatively cambered wings. The result suggest that active pitch control in combination with leading edge and chord-wise flexibility is likely to produce effective aerodynamic outcomes.

I. Introduction

Natural flyers and swimmers commonly exhibit wing (or tail) passive and active rotation about a leading edge skeletal structure. In birds, this leading edge skeletal structure naturally promotes wing chord-wise alignment with the flow, or feathering, and is responsible for generating passive (and active) wing rotation about the leading edge and wing deformation. Similarly, bats have a main arm and wrist skeletal structure at their wing leading edge that generates a similar passive (and active) structural deformation. Both birds and bats also have muscles that can control the degree to which leading edge rotates as well as the shape of the wing. This leading edge dominant skeletal structure is of interest for several reasons. First, by understanding this structural strategy, it may be better leveraged and mimicked by small human made ornithopers. Understanding this aero-structure interaction may prove effective in improving system flight efficiency and maneuverability. Second, these structural strategies have what appears to be a natural gust

[*]Graduate Student, University of Massachusetts, Lowell

[†]Undergraduate Student, University of Massachusetts, Lowell

[‡]Associate Professor, Senior AIAA member

[§]Associate Professor, Senior AIAA member

[¶]Associate Professor, Senior AIAA member

alleviation and stable force modulation capability; wherein, the wing rotation increases as loads increase, thereby tempering sudden increases in aerodynamics forces.

In addition to examining the aero-structural response of this wing-skeletal structure, this paper examines the development and persistence of the leading-edge vortex (LEV). LEVs are common flow structures used to augment lift in low-Reynolds number flight and swimming applications. Much previous work has examined LEVs, both in pitch-ramp-return wing dynamics[?,1,2] and pitched plate experiments.[?,?]

The research question that is explored in this paper is: how does a single degree of freedom (DOF), passive leading edge compliance (rotational stiffness about the leading edge) impact the development and persistence of LEVs? In addition, this paper will explore how different structural strategies result in different control inputs from control systems such as muscles or actuators when the same or similar flowfield/force time history is desired.

II. Methods

This section briefly describes the computational and experimental methods used in this paper. Since many of these methods have been previously described in detail in previous papers, only an overview is given here.

A. Low-fidelity, Unsteady Potential Flow Solver

The majority of this study is performed using an in-house, low-fidelity computational tool[3] which strongly couples the aerodynamics forces and the structural dynamic response of a simple two-dimensional airfoil. The airfoil is a thin surface with camber prescribed using a polynomial and prescribed leading edge (and trailing edge) angle. This computational tool was described in detail in Willis et al.,[3] and is only briefly introduced in this paper.

The unsteady aerodynamics model uses a two-dimensional potential flow method to predict the forces and moments. This potential flow tool is a doublet lattice panel method (DLPM) with linear strength panels to represent the airfoil and the unsteady wake shedding. The trailing edge wake shedding strength is determined at each time-step using a traditional Kutta condition. The leading-edge vorticity shedding strength is determined at each flow evaluation step using a Leading-Edge Shedding Parameter.[2,6] The wake is represented using linear strength doublet panels whose positions are updated at each flow evaluation step using a two-step, Runge-Kutta predictor-corrector method.[9]

The structural dynamics model uses a single torsional spring-mass-damper model. This single point structural model is strongly coupled with the leading edge aerodynamic moment to capture the passive fluid structure interactions. A Newton method solver is used to resolve the moment balance at the leading edge of the wing. typically, the structural dynamics and aerodynamic moments at the leading edge are in balance within 15-20 Newton steps.

This computational tool has two modes of operation, a forward evaluation and a quasi-inverse design formulation. Only the forward evaluation tool is used in this paper. The forward evaluation or solution approach is outlined in the flow chart shown in Figure 1. The approach uses a known spring constant and known leading edge dynamics to calculate the aerodynamics forces/moments and thus resulting angular deflection of the wing. The result of this computation is a certain leading edge shedding rate (at each timestep) and the formation, development and persistence of the leading edge vortex is largely a result of the prescribed spring constant and kinematics.

B. High Fidelity Simulations

The high fidelity simulations are performed using 3DG, a High Order discontinuous Galerkin Navier Stokes Solver.[8] In these simulations, the solver uses prescribed airfoil motions from the low fidelity model as kinematics inputs and simply solves for the flow-field around the prescribed geometry and motions. The model itself, does not include the fluid-structure interaction at the leading edge.

C. Water Tank Experiments

A series of fluid-structure interaction wing experiments were performed at University of Maryland Water Tow Tank Facility. These experiments have been reported in previous literature.[4,5]

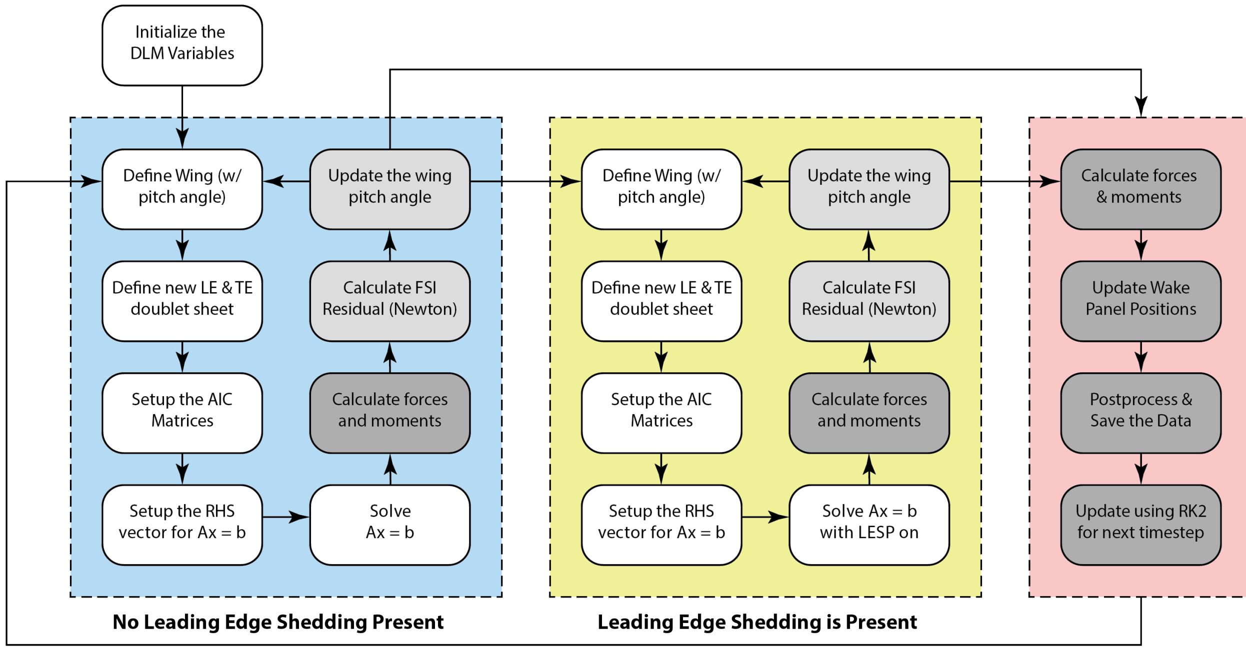

Figure 1. The forward evaluation flow chart.

III. Computational Experiment Cases

The airfoil kinematics which are examined are similar to those presented in Jones et al.[4,5] and Willis et al.[3] These in-lab and computational experiments examine a wing, set at an initial incidence angle in a quiescent fluid. The wing is then accelerated (constant acceleration) over a given acceleration distance ($a_{a/c} = 2.0$) to reach the final speed, U_f. At that point, the wing continues to translate at a constant velocity for the remainder of the case. The results are reported in non-dimensional form.

Four computational experiments are presented in this paper, with the specific details for each shown in tables 1-2 :

1. **Computational Experiment 1: Baseline Experiment & Computation Cases**: This series of four test cases compares the original water tow tank experiments,[4,5] high fidelity CFD[8] and the low fidelity DLPM computational tool. The purpose of these experiments is to examine the validity of the low fidelity potential flow solution method for modeling highly separated viscous flows.

2. **Computational Experiment 2: Rigid Wing Cases, Different Incidence Angles** : This series of computational cases examines airfoils without a structurally compliant leading edge. The purpose of these experiments is to examine how rigid, single incidence angle wings shed vorticity into the LEV structure. These experiments were performed using the DLPM low-fidelity tool without the structure being coupled to the flow solution.

3. **Computational Experiment 3: Compliant Leading Edge, Initial Incidence** 60 **deg.**: This series of computational cases introduces leading edge compliance and camber at a high initial wing incidence. Here, the initial wing incidence angle is 60 degrees. This initial angle represents the zero structural moment angle or the force free equilibrium position. The wing is massless and dynamic system damping is set to zero for these cases. The purpose of these experiments is two-fold (a) to determine whether/how structural compliance affects the development and persistence of the leading edge vortex and (b) to determine how wing camber can impact the development and persistence of the leading edge vortex.

4. **Computational Experiment 4: Compliant Leading Edge, Initial Incidence** 45 **deg.**: This series of computational cases introduces leading edge compliance and camber at a moderate initial wing incidence of 45 degrees. The purpose of these experiments is to further support and compare trends with the results in Computational Experiment 3.

Table 1. **The computational experiment case parameters used in the present study.**

	Airfoil Camber	**Computational Tools**
Comp. Exp. 1	None	DLPM, 3DG, Experiment
Comp. Exp. 2	None	DLPM
Comp. Exp. 3	None, Positive & Negative Camber	DLPM
Comp. Exp. 4	None, Positive & Negative Camber	DLPM

Table 2. **The computational experiment case parameters used in the present study.**

	Spring Constant, N-m/rad per unit span	**Initial Angle** deg.
Comp. Exp. 1	k = ∞, k = 0.3220 and k = 0.1288, k = 0.000	60 deg.
Comp. Exp. 2	None	20,30,40,50,60 deg.
Comp. Exp. 3	k = 0.050, 0.100, 0.150, 0.200, 0.250, 0.300, 0.350, 0.400, 0.450, 0.500	60 deg.
Comp. Exp. 4	k = 0.050, 0.100, 0.150, 0.200, 0.250, 0.300, 0.350, 0.400, 0.450, 0.500	45 deg.

IV. Computational Results

?

A. Results: Computational Experiment 1

In this first series of tests cases, the low-fidelity model is compared with experimental results as well as high-fidelity simulations. For this comparison, the low fidelity solver is used to determine the fluid-structure interactions and resulting wing kinematics, while the high fidelity solver uses these pre-solved wing incidence angles as the pre-prescribed wing position and angle. This by nature allows us to compare the flow-fields determined from the two computational methods in a more consistent and direct manner. Because the fluid-structure interaction is not directly determined in the high fidelity solver, but rather prescribed from the lower-fidelity results, the differences observed should be due to flow physics and fidelity of the computational methods alone.

The normal force production results are shown in Figure 2 and illustrate reasonable agreement between the the different representations of the same case. The comparison of experimental and low-fidelity results was previously presented in Willis et. al.[3] and a detailed discussion can be seen in that work. The high fidelity computational results show reasonably good trend with the low-fidelity and experiment results in particular during the initial period where the LEV first develops and becomes mature ($0 < t^* < 5.0$). This supports the hypothesis that a potential flow model can capture the significant aerodynamics behaviors in initial LEV development.

Flow visualization results for the doublet lattice panel method (DLPM) are shown adjacent to the high fidelity model flow simulation visualization for a rigid wing held at 60 degrees, a stiff spring, a weak spring and no spring in Figures 3 - 6. The flow visualizations show good trend similarity across the range of computations performed. The rigid wing cases (Figure 3) show good agreement between the high-fidelity and low-fidelity representations, with the LEV development and core in similar regions. The compliant leading edge cases (Figure 4 and Figure 5) show good visual agreement between the low- and high-fidelity representations until flow separation has taken place. In both of these cases, a secondary vortex is also seen developing close to the leading edge of the airfoil. This secondary vortex is viscous in nature and is not present in the low fidelity solver. While this secondary vortex likely plays a role in the LEV development and persistence, the low fidelity solver is able to still predict the flow well for the first $t^* = 4.0 - 5.0$ dimensionless time units.

Finally, the no-spring case shown in Figure 6, shows good agreement again between the low fidelity and high fidelity solutions. The LEV develops, translates and sheds from the wing at a faster rate in the low-fidelity solver than in the higher-fidelity solver. It is possible that, once again, viscous effects not modeled in the lower-fidelity tool may play a role in this difference. ?

B. Results: Computational Experiment 2: Rigid Wing Test Cases

This series of test cases examines the wing when it is held at a single incidence angle ($20, 30, 40, 50$ and 60 degrees) for the duration of the computational experiment. This is akin to a rigid wing set to a single incidence angle for the duration of the translational motion.

The lift and drag coefficients (Figure 7) are similarly behaved during the wing acceleration ($t^* < 4.0$) for all incidence angles considered; however, these force coefficients exhibit some subtle differences once the wing reaches a steady velocity. At lower incidence angles (20 and 30 degree cases), the lift and drag coefficients continue to rise, until they reach a maximum between $t^* = 4.75$ and $t^* = 5.10$. After this, the lift production drops relatively quickly and becomes less consistent. Conversely, the higher incidence angle cases (50 and 60 degrees) show that the maximum lift coefficient is achieved soon after the acceleration phase is complete ($t^* > 4.0$) and gradually decreases. There does not appear to be as rapid or sudden loss of lift, implying that the LEV augmentation of the lift and drag forces is maintained throughout the time considered ($0 < t^* < 5.97$).

The flow-field results are shown in Figure 8 through 13. The 20-degree incidence angle case visually shows some instability forming in the LEV between the flow-field snapshots taken at $t^* \simeq 4.69 - 5.15$. This is consistent with the decline observed in the force coefficient production in Figure 7 for this case. The higher angle of attack cases show a well-formed vortex for the duration of the cases. This is consistent with the persistence of the high lift (and drag) coefficients reported in Figure 7.

The results of the rigid wing test cases illustrate that higher incidence angles tend to produce more consistent and persistent LEV behavior. These results also indicate that the force coefficients produced at higher incidence angles have only gradual changes (reductions) after the wing has completed the acceleration phase.

?

C. Results: Computational Experiment 3: Compliant Leading Edge Cases, 60 deg.

In this third series of test cases, we explore how the leading edge spring compliance impacts the evolution and persistence of the leading edge vortex. The wing is set to an initial incidence angle of 60 degrees with zero leading edge moment contribution from the torsional spring. We also examine how camber affects the persistence of the LEV. Here, a polynomial representation is used for the wing, with camber being defined based on the leading edge angle ($\theta = -10, 0, 10$ degrees). For this computational experiment, ten different leading edge spring constants are modeled for each wing camber, for a total of 30 different computational test cases. The lift and drag evolution of each case is shown in (Figure 14). Similarly, the LEV flow-field evolution is also shown in Figure 15 through Figure 20, with all 30 results shown for a single time-step together.

The lift and drag coefficient evolution for these cases, presented in Figure 14, suggest that the magnitude of the leading edge torsional spring constant can have a considerable impact on force coefficient evolution as well as the time (t^*) where the peak lift and drag is observed. For low spring constants, $k = 0.05 - 0.15$, the wing reaches a local maximum lift soon after the acceleration phase is completed ($t^* = 4.0$). The lift (and drag) values decrease for $t^* \simeq 0.75 - 0.80$, before beginning to increase or recover. The higher spring constant cases show a consistent and gradual force coefficient increase until $t^* > 5.0$, indicating the force coefficient augmentation by the LEV has persisted for a longer period of time. Despite this longer persistence of the force coefficients, the force drop-off is similar to those lower incidence angle rigid wing cases presented in Figure 7. This is not surprising as the leading edge compliance has a feathering effect on the wing, and thus reduces the incidence angle. The lift and drag coefficients are slightly effected by the wing camber, with positive camber wings having a slightly higher lift generating capability than flat or rigid wings. This result is consistent with traditional, steady aerodynamics theories and observations.

To gain deeper insight, the LEV development is also visualized (Figure 8 through Figure 13) for a collection of time-steps representing the airfoil completing the acceleration phase and reaching a steady state translational velocity ($t^* = 3.84 - 5.97$). These flow-field visualizations illustrate how the force coefficient evolution is impacted by the LEV development and persistence above the wing. A visual identification of vortex separation was performed for each of the cases, and a summary of the LEV persistence is presented in Figure **??**. Cases with lower spring constants ($k = 0.050, 0.100, 0.150$) show smaller LEV's forming with earlier LEV separation from the wing. This is consistent with the lower incidence angles that form with the flow when the leading edge has significant compliance. This same behavior was noted for the rigid wing cases a lower incidence angles to the flow. The results also show that a significant majority of the compliant leading edge airfoils had LEVs that had separated before $t^* = 6.0$, despite some of these airfoils having relatively large incidence angles.

The results in Figure **??** also show how wing camber impacts the LEV persistence. The more positive camber cases, have slightly shorter LEV persistence while negative camber cases show slightly longer LEV persistence.

?

D. Results: Computational Experiment 4: Compliant Leading Edge Cases, 45 deg.

In the Figure 21, similar results are presented, but now for an initial wing incidence angle of 45 degrees. Once again the lift and drag coefficient evolution shows different trends between lower spring constants ($k = 0.050, 0.100, 0.150$) and stiffer spring constants, particularly after the initial airfoil acceleration phase is complete. The behavior is similar to that observed when the initial incidence angle was greater (60 degrees).

Once again, the flow-field results are also presented in Figure 22 through Figure 27. The results here are only shown for the flat plate and positive camber airfoil. Similar trends are observed once again for the 45 degree initial incidence as are observed for the 60 degree initial incidence.

V. Discussion

This section briefly discusses the effect of leading edge compliance and airfoil camber on the persistence of the leading edge vortex (LEV).

A. Low Fidelity Computational Tool

The low fidelity, two-dimensional doublet lattice panel method continues to show good trend agreement during initial LEV development stages with both high fidelity 2D computations as well as three-dimensional wing tow tank experiments. The low fidelity tool does continue to show divergent results when the LEV separates (or is close to separating). Similarly, the low fidelity method is incapable of capturing secondary vortex formation within the LEV, which will undoubtedly play some role in the overall LEV persistence and development. The results of the low-fidelity solver should still be used with caution, but, can likely be used as a preliminary prediction tool for initial LEV development to save computational effort in higher fidelity tools.

B. Effect of Leading Edge Structural Compliance on LEV persistence

The computations performed in this paper show that leading edge compliance can play a significant role in the development and persistence of a leading edge vortex above an airfoil at high incidence angle. The computed results show that lower spring constants (high levels of leading edge compliance) result in early LEV separation and lower persistence. This is not a surprising result, as wings with high leading edge compliance will tend to align more with the flow than those with a stiffer leading edge. As a result of this lower wing incidence, the vorticity shedding from the leading edge will have a lower magnitude and therefore, will have a lower tendency to stay attached to the wing. Additionally, the lower wing incidence angle to the flow will result in a weaker LEV that will ultimately have difficulty persisting on the suction surface of the airfoil. Stiffer (lower compliance) leading edges tend to encourage longer vortex persistence on the wing. In the limit that the leading edge approaches that of a rigid wing, the LEV will continue to persist. Ultimately, passive leading edge compliance, in these computational cases, results in shorter duration of LEV persistence.

While higher levels of structural compliance in this computational experiment are associated with shorter duration LEV persistence above the wing, one should bear in mind that natural flyers tend to have active musculature that can be used to both tune the compliant nature of the wing as well as increase the baseline equilibrium angle for that compliance. As such, it is likely that these natural flyers make active adjustments to their wing shape and equivalent compliance to achieve the desired flight characteristics.

C. Effect of camber on LEV Persistence

Many natural flyers have lightweight wing structures that could result in significant passive deformation during flapping motions. The computational study of how camber affects LEV persistence was undertaken to explore how this passive wing morphing ("de-cambering") might affect the LEV persistence on natural wings. The computational results showed that positive wing camber, when prescribed, had a small, but negative effect on the persistence of LEVs on the wing suction surface. Conversely, negative camber was associated with slightly longer LEV persistence. It is hypothesized that the negative camber resulted in two advantageous effects, (1) the negative camber provides more "physical space" for the LEV to develop above the wing, allowing the vortex to grow with less impact on the surrounding flow and (2) the airfoil leading edge presented by a negatively cambered wing would appear to be sharper (or have a higher adverse pressure gradient) than a positively cambered wing, thus resulting in stronger shear layers shedding into the flow. These combined effects of wing camber have a small, but noticeable effect on the LEV development.

In natural flyers, the compliant wing is likely to undergo some level of de-cambering during the high force production downstroke phase of the wing beat cycle. As a result, the wing will likely naturally create a slightly positive impact on the LEV development. We plan to explore the impact of this passive wing shape change in the near future.

VI. Conclusions

This paper presented the results of a computational study that was primarily performed using a two-dimensional, doublet lattice method, low fidelity computational tool. Based on the cases run in this paper, the following conclusions were made:

1. The low fidelity, doublet lattice panel method computational tool continues to show promise for predicting trends in LEV dominated flows.

2. For the cases examined, *passive* leading edge compliance is associated with a shorter persistence of the leading edge vortex due to the feathering effect of leading edge compliance. It is anticipated that *active* modulation of the structural compliance may have a positive impact on the development and persistence of the LEV.

3. For the cases examined, positive camber has a slightly negative impact on the persistence of the leading edge vortex. In the cases examined, those airfoils with negative camber had longer LEV persistence, all things being equal.

VII. Acknowledgements

This material is based upon work supported by the National Science Foundation under Grants No. 1511507. Any opinions, findings, and conclusions or recommendations expressed in this material are those of the author(s) and do not necessarily reflect the views of the National Science Foundation.

References

[1]Toomey, J., & Eldredge, J. D. (2008). Numerical and experimental study of the fluid dynamics of a flapping wing with low order flexibility. Physics of Fluids, 20(7), 073603.

[2]Ramesh, K., Gopalarathnam, A., Granlund, K., Ol, M., & Edwards, J. (2014). Discrete-vortex method with novel shedding criterion for unsteady aerofoil flows with intermittent leading-edge vortex shedding. Journal of Fluid Mechanics, 751, 500-538. doi:10.1017/jfm.2014.297

[3]Willis, D. J., Anwar, M.I., Gowda, R.B.V., Manar, F. & Jones, A.R. (2018). An Unsteady Doublet Lattice Method for Studying LEV Development on Low-Re Wings with Leading Edge Compliance with Experimental Comparison. AIAA 2018-0312, In 31st AIAA Scitech Conference, 2018.

[4]Manar, F., Cassell, M., & Jones, A. R. (2016). The Response of a Single Degree-of-Freedom Wing at Low Reynolds Number. In 46th AIAA Fluid Dynamics Conference (p. 3633).

[5]Manar, F., & Jones, A. R. (2017). Vorticity Production at the Leading Edge of Flat Plates at High Incidence. In 55th AIAA Aerospace Sciences Meeting (p. 0545).

[6]Ramesh, K., Gopalarathnam, A., Ol, M. V., Granlund, K., & Edwards, J. R. (2011). Augmentation of inviscid airfoil theory to predict and model 2d unsteady vortex dominated flows. AIAA Paper, 3578, 2011.

[7]Ramesh, K., Gopalarathnam, A., Edwards, J. R., Ol, M. V., & Granlund, K. (2013). An unsteady airfoil theory applied to pitching motions validated against experiment and computation. Theoretical and Computational Fluid Dynamics, 27(6), 843-864.

[8]Persson, P.-O., Willis, D.J. & Peraire, J. (2012), Numerical simulation of flapping wings using a panel method and a high-order Navier-Stokes solver. Int. J. Numer. Meth. Engng, 89: 12961316. doi:10.1002/nme.3288

[9]Butcher, J. C. (1987). The numerical analysis of ordinary differential equations: Runge-Kutta and general linear methods. Wiley-Interscience.

[10]Mountcastle, A. M., & Daniel, T. L. (2009). Aerodynamic and functional consequences of wing compliance. Experiments in fluids, 46(5), 873.

[11]Bahlman, J. W., Swartz, S. M., & Breuer, K. S. (2013). Design and characterization of a multi-articulated robotic bat wing. Bioinspiration & biomimetics, 8(1), 016009.

[12]Song, A., Tian, X., Israeli, E., Galvao, R., Bishop, K., Swartz, S., & Breuer, K. (2008). Aeromechanics of membrane wings with implications for animal flight. AIAA journal, 46(8), 2096.

[13]Curet, O. M., Carrere, A., Waldman, R., & Breuer, K. S. (2014). Aerodynamic characterization of a wing membrane with variable compliance. AIAA journal.

[14]Katz, J., & Plotkin, A. (2001). Low-speed aerodynamics (Vol. 13). Cambridge university press.

[15]Willis, D. J., Peraire, J., & White, J. K. (2007). A combined pFFTmultipole tree code, unsteady panel method with vortex particle wakes. International Journal for numerical methods in fluids, 53(8), 1399-1422.

[16]Stroud, A. H., & Secrest, D. (1966). Gaussian quadrature formulas.

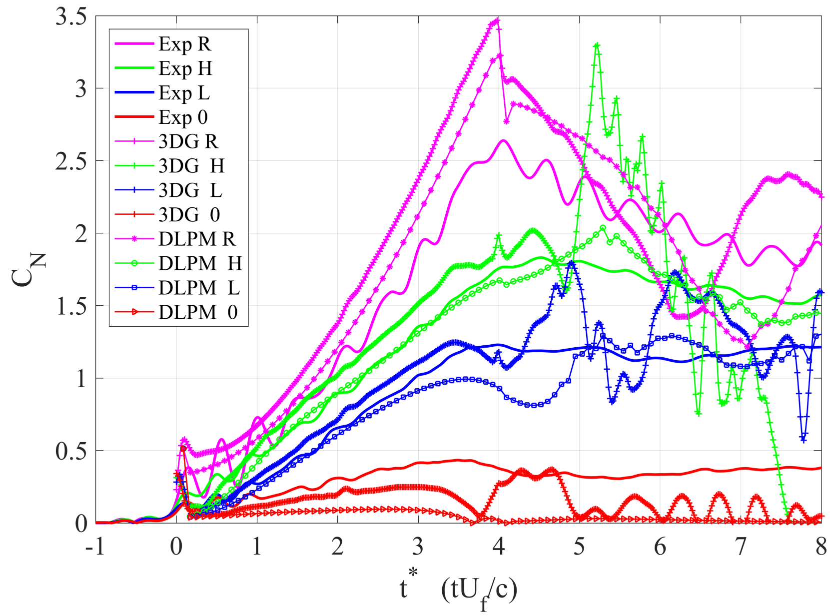

Figure 2. A comparison of the normal force coefficient production with respect to time for (a) Water tank experiment, (b) high fidelity simulation and (c) Low fidelity simulation.

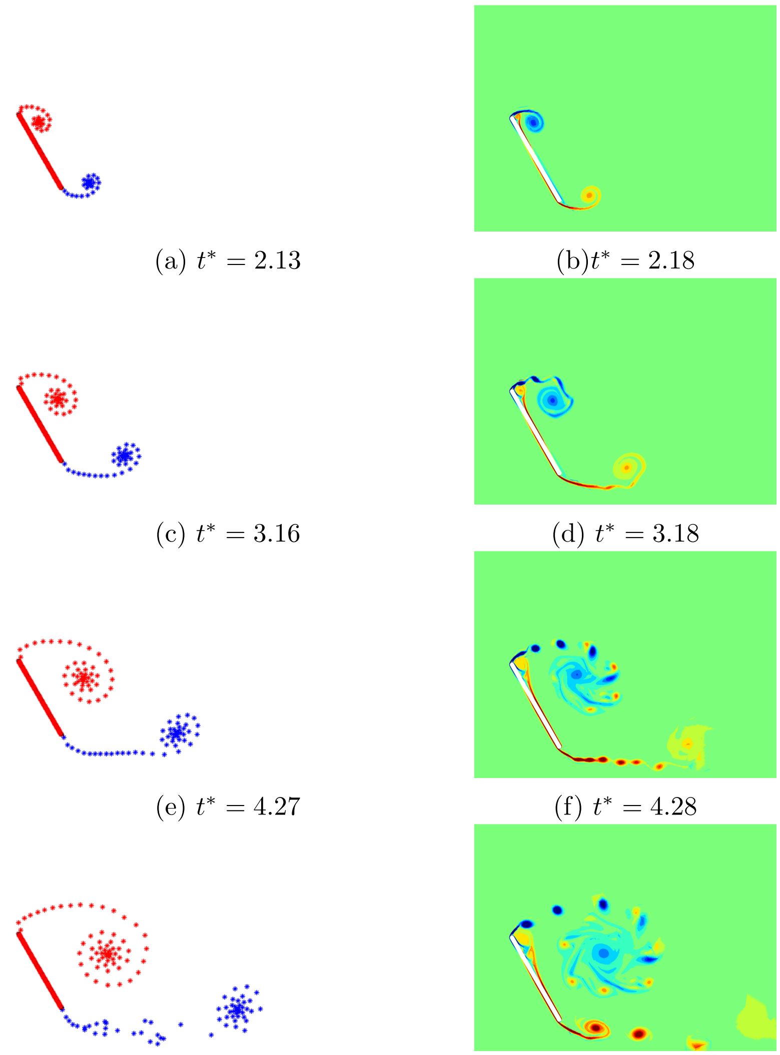

(a) $t^* = 2.13$ (b)$t^* = 2.18$

(c) $t^* = 3.16$ (d) $t^* = 3.18$

(e) $t^* = 4.27$ (f) $t^* = 4.28$

(g) $t^* = 5.29$ (h) $t^* = 5.28$

Figure 3. A comparison of the vortex development between the doublet lattice method (left column) and the 3DG high fidelity simulation tool (right column) for the rigid leading edge case at similar times.

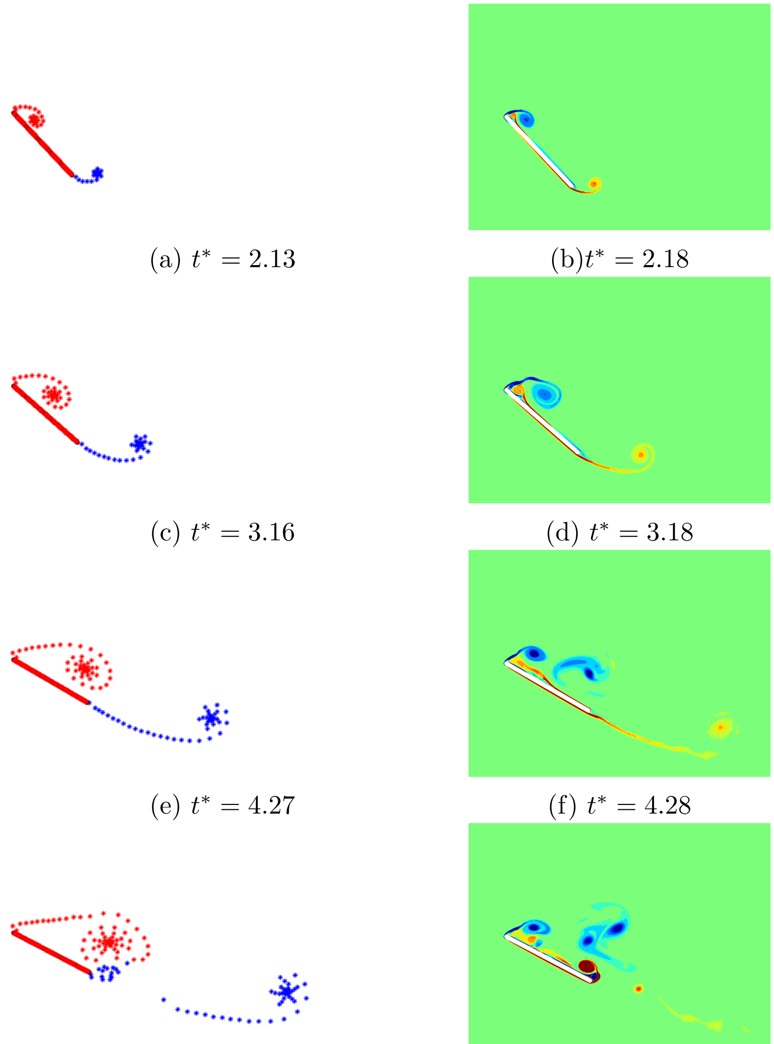

(a) $t^* = 2.13$ (b)$t^* = 2.18$

(c) $t^* = 3.16$ (d) $t^* = 3.18$

(e) $t^* = 4.27$ (f) $t^* = 4.28$

(g) $t^* = 5.29$ (h) $t^* = 5.28$

Figure 4. A comparison of the vortex development between the doublet lattice method (left column) and the 3DG high fidelity simulation tool (right column) for the stiff leading edge spring ($k = 0.322$) at similar times.

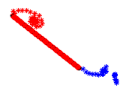
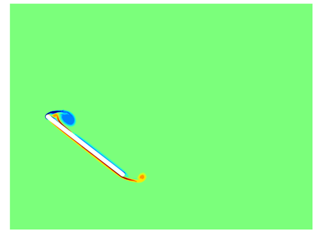

(a) $t^* = 2.13$ (b)$t^* = 2.18$

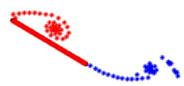
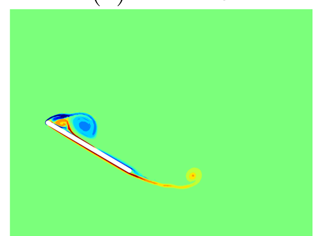

(c) $t^* = 3.16$ (d) $t^* = 3.18$

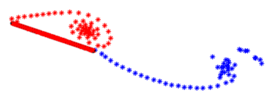
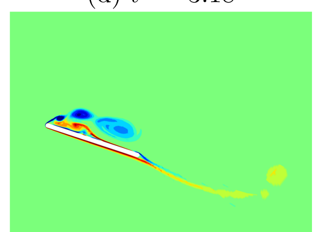

(e) $t^* = 4.27$ (f) $t^* = 4.28$

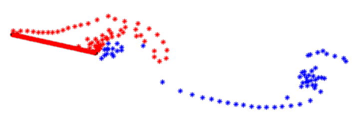
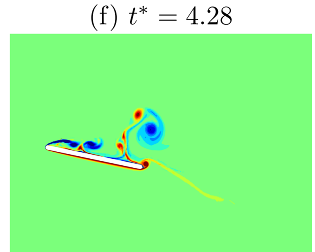

(g) $t^* = 5.29$ (h) $t^* = 5.28$

Figure 5. A comparison of the vortex development between the doublet lattice method (left column) and the 3DG high fidelity simulation tool (right column) for the weak leading edge spring ($k = 0.1288$) at similar times.

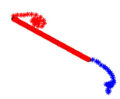

(a) $t^* = 2.13$

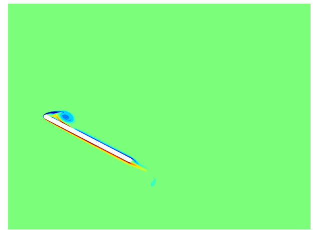

(b)$t^* = 2.18$

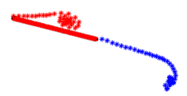

(c) $t^* = 3.16$

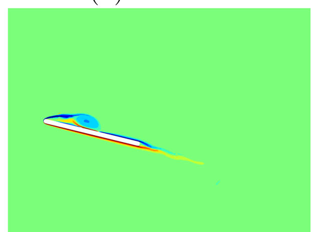

(d) $t^* = 3.18$

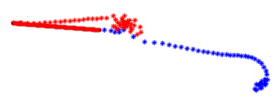

(e) $t^* = 4.27$

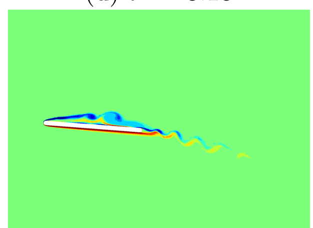

(f) $t^* = 4.28$

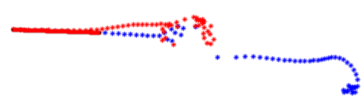

(g) $t^* = 5.29$

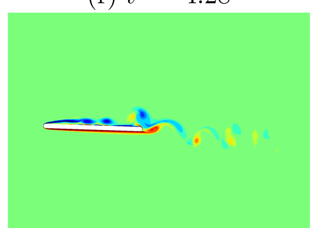

(h) $t^* = 5.28$

Figure 6. A comparison of the vortex development between the doublet lattice method (left column) and the 3DG high fidelity simulation tool (right column) for the no leading edge spring ($k = 0.000$) at similar times.

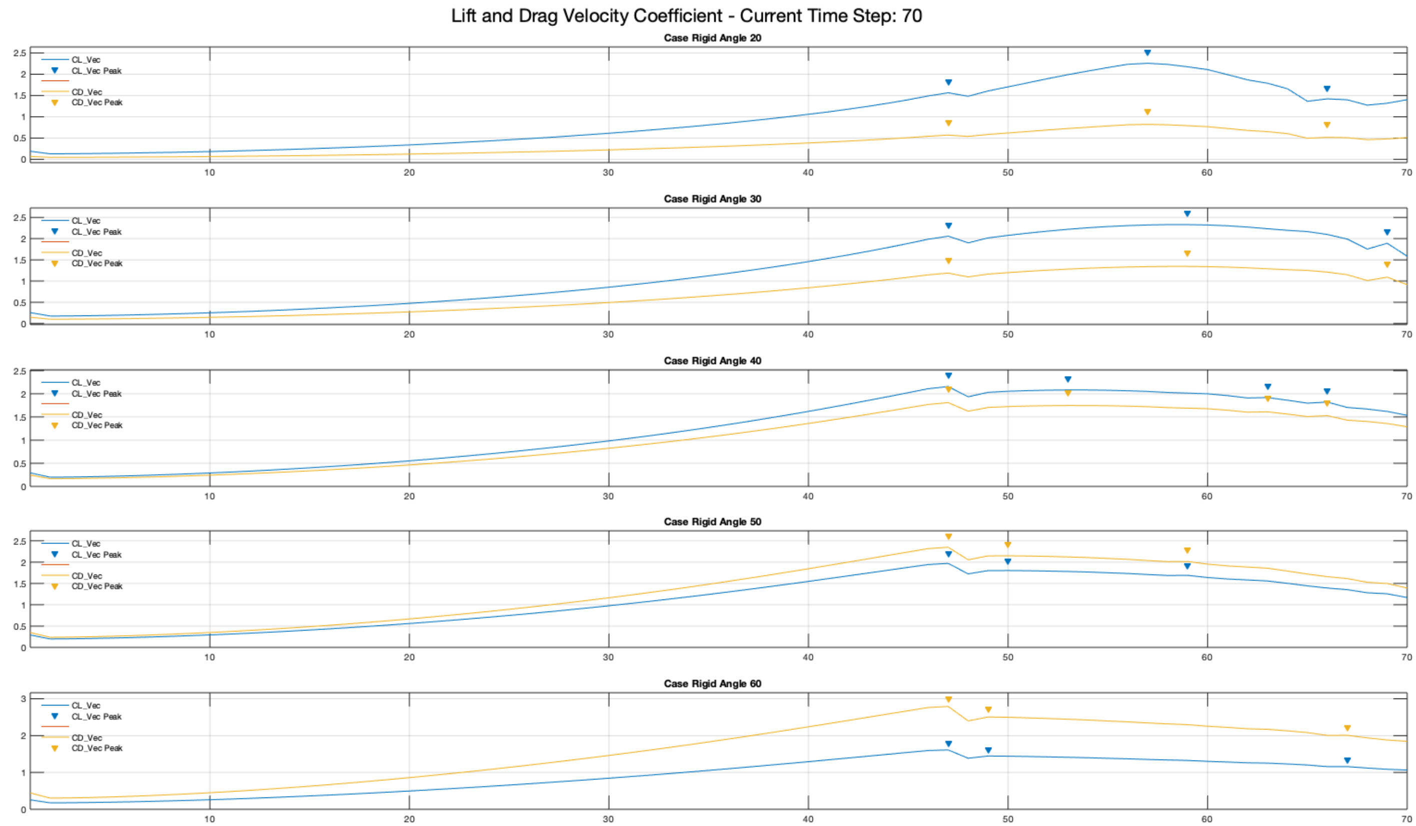

Figure 7. Lift and Drag Coefficient evolution with respect to time-step for a rigid flat plate held at a single incidence angle to the flow.

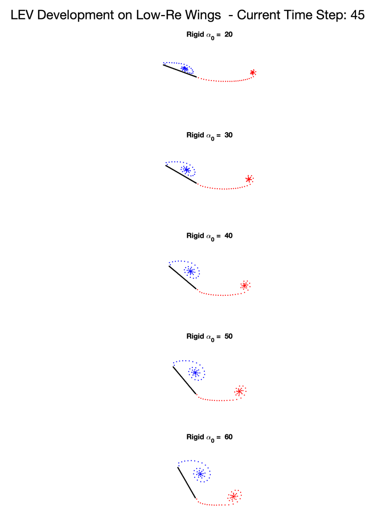

Figure 8. Lift and Drag Coefficient evolution with respect to time-step, for a rigid flat plate held at a single incidence angle to the flow, $t^* = 3.84$.

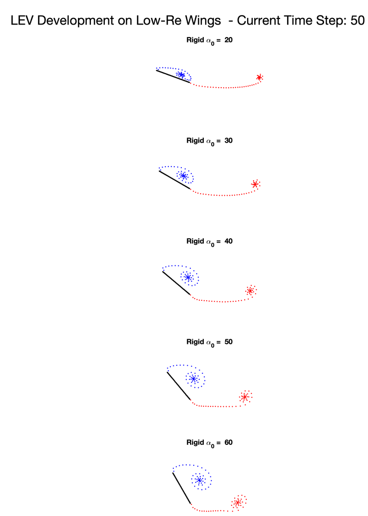

Figure 9. Lift and Drag Coefficient evolution with respect to time-step, for a rigid flat plate held at a single incidence angle to the flow, $t^* = 4.27$.

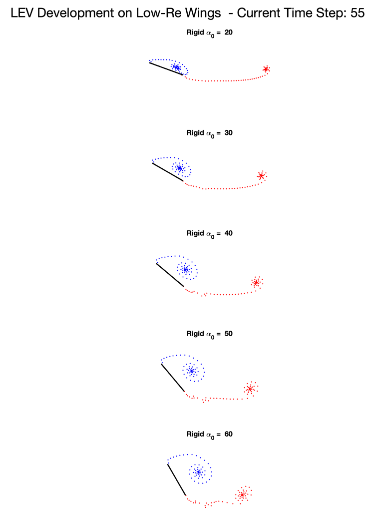

Figure 10. Lift and Drag Coefficient evolution with respect to time-step, for a rigid flat plate held at a single incidence angle to the flow, $t^* = 4.69$.

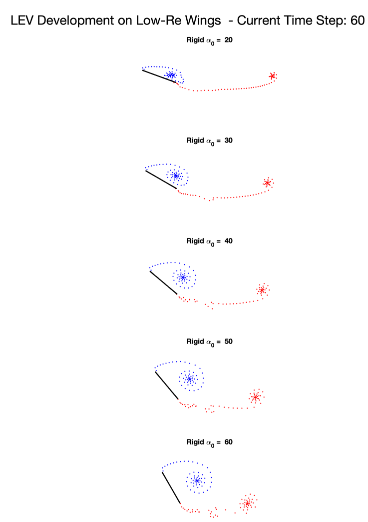

Figure 11. Lift and Drag Coefficient evolution with respect to time-step, for a rigid flat plate held at a single incidence angle to the flow, $t^* = 5.12$.

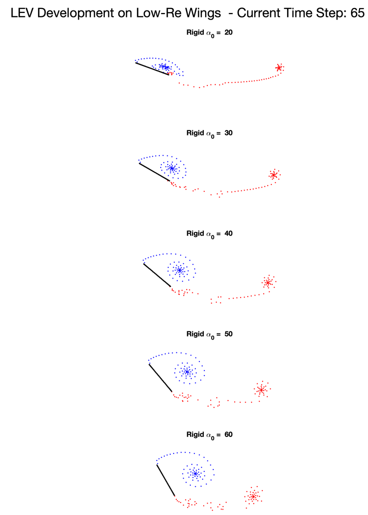

Figure 12. Lift and Drag Coefficient evolution with respect to time-step, for a rigid flat plate held at a single incidence angle to the flow, $t^* = 5.54$.

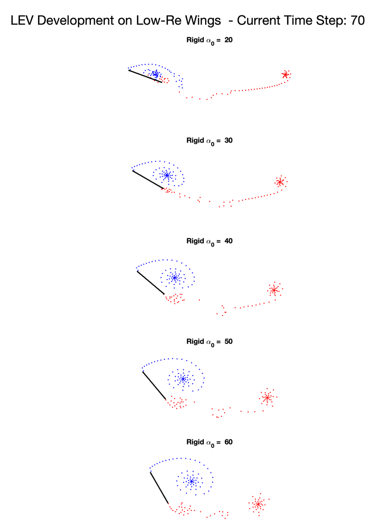

Figure 13. Lift and Drag Coefficient evolution with respect to time-step, for a rigid flat plate held at a single incidence angle to the flow, $t^* = 5.97$.

Figure 14. Lift and Drag Coefficient evolution with respect to time-step, with initial incidence angle of 60 degrees and different spring constants.

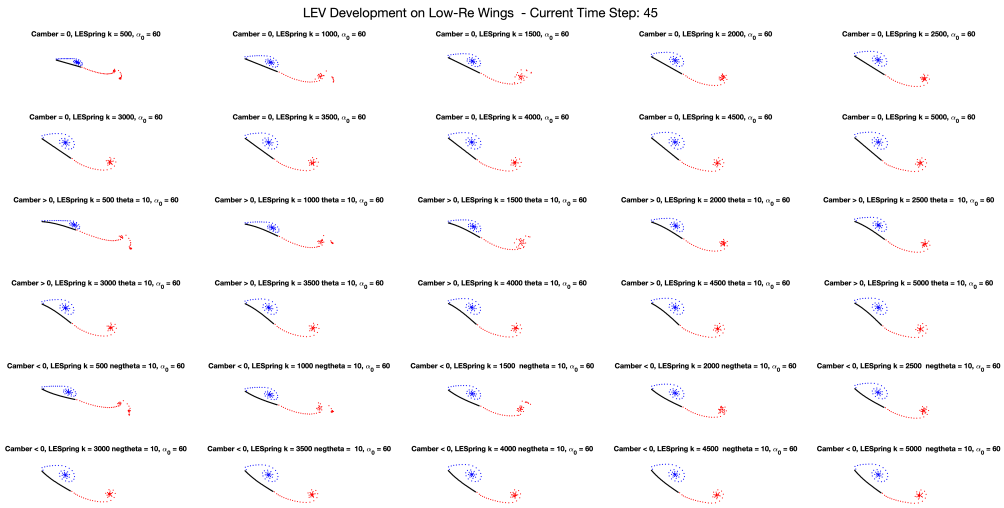

Figure 15. Lift and Drag Coefficient evolution with respect to time-step, with initial incidence angle of 60 degrees and different spring constants, $t^* = 3.84$.

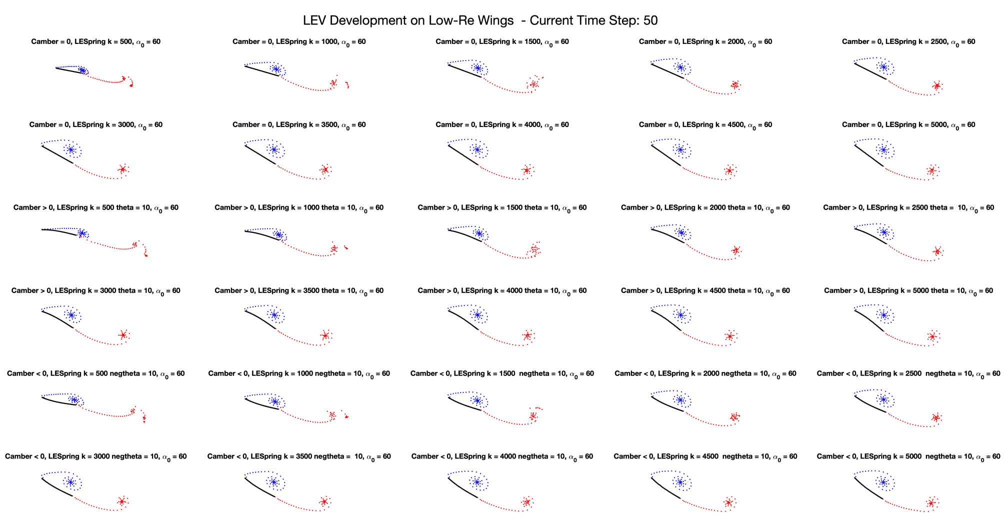

Figure 16. Lift and Drag Coefficient evolution with respect to time-step, with initial incidence angle of 60 degrees and different spring constants, $t^* = 4.27$.

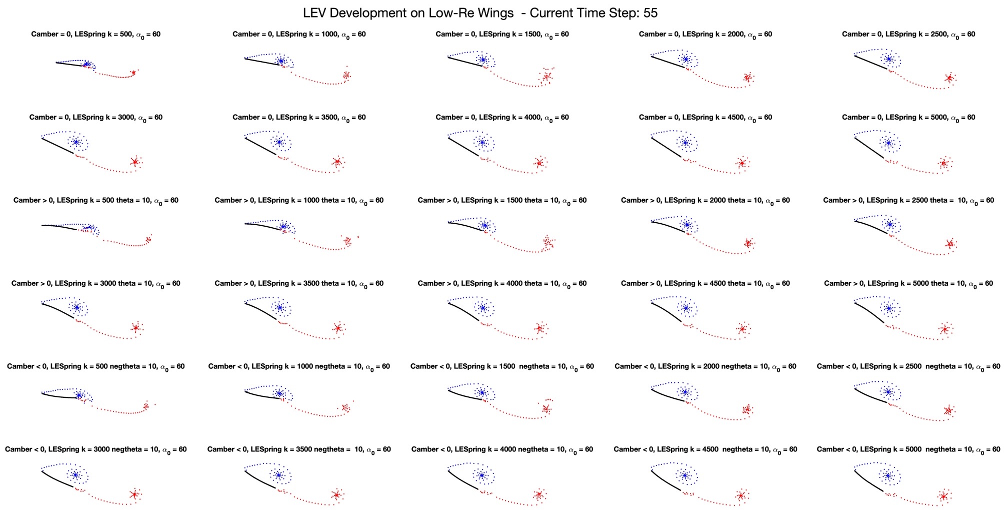

Figure 17. Lift and Drag Coefficient evolution with respect to time-step, with initial incidence angle of 60 degrees and different spring constants, $t^* = 4.69$.

Figure 18. Lift and Drag Coefficient evolution with respect to time-step, with initial incidence angle of 60 degrees and different spring constants, $t^* = 5.12$.

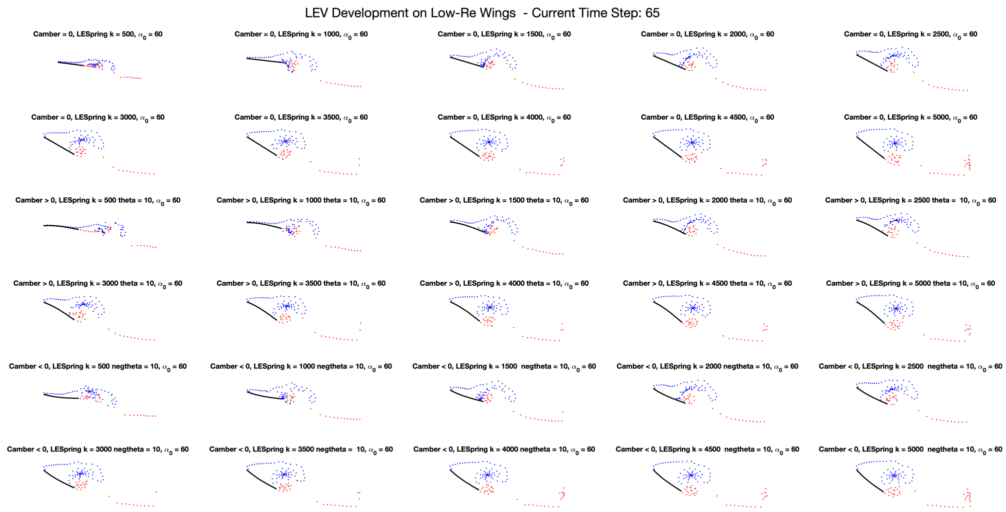

Figure 19. Lift and Drag Coefficient evolution with respect to time-step, with initial incidence angle of 60 degrees and different spring constants, $t^* = 5.54$.

Figure 20. Lift and Drag Coefficient evolution with respect to time-step, with initial incidence angle of 60 degrees and different spring constants, $t^* = 5.97$.

Figure 21. Lift and Drag Coefficient evolution with respect to time-step, with initial incidence angle of 45 degrees and different spring constants.

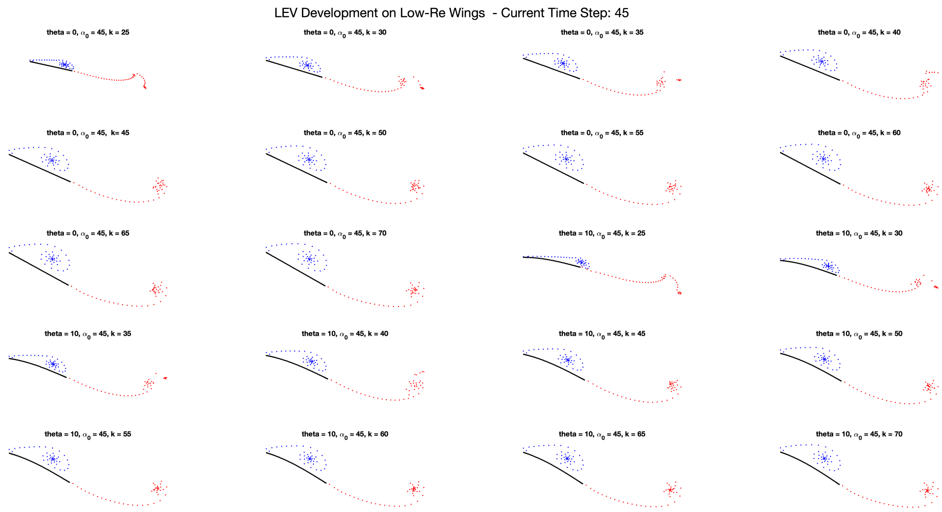

Figure 22. Lift and Drag Coefficient evolution with respect to time-step, with initial incidence angle of 45 degrees and different spring constants, $t^* = 3.84$.

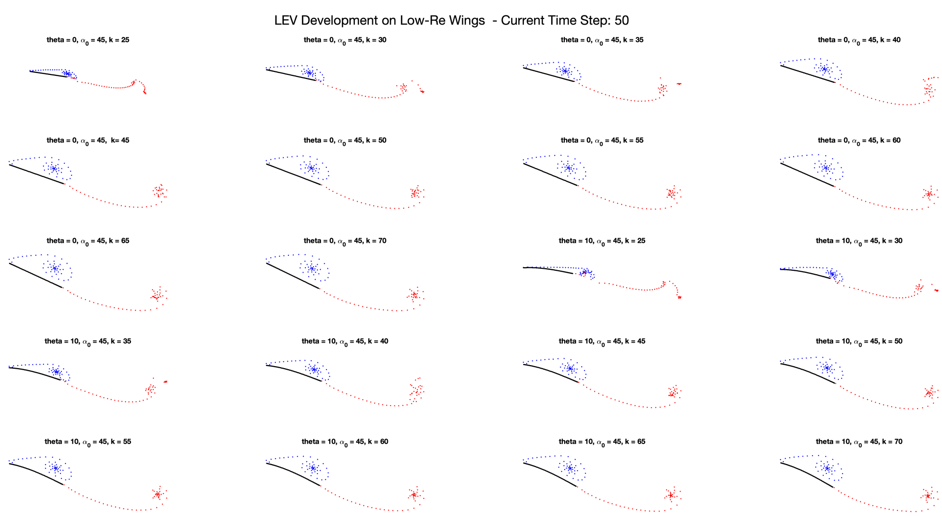

Figure 23. Lift and Drag Coefficient evolution with respect to time-step, with initial incidence angle of 45 degrees and different spring constants, $t^* = 4.27$.

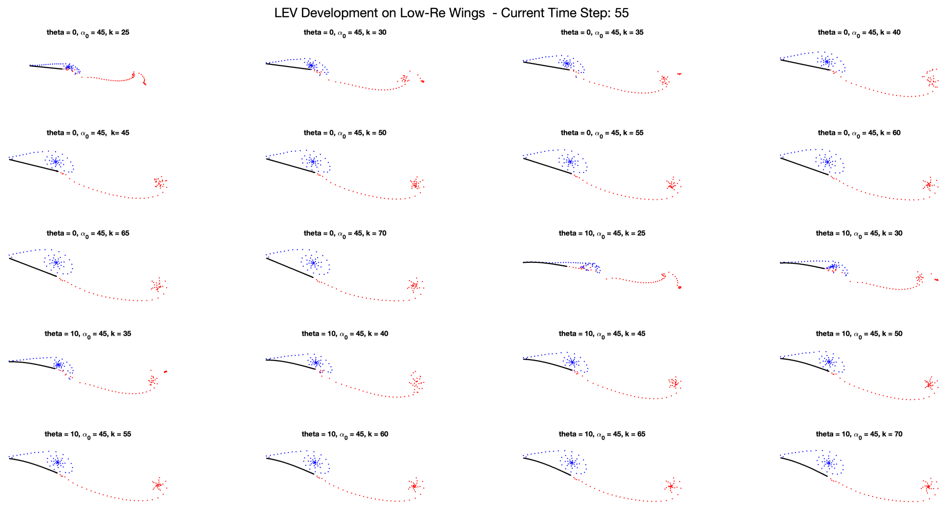

Figure 24. Lift and Drag Coefficient evolution with respect to time-step, with initial incidence angle of 45 degrees and different spring constants, $t^* = 4.69$.

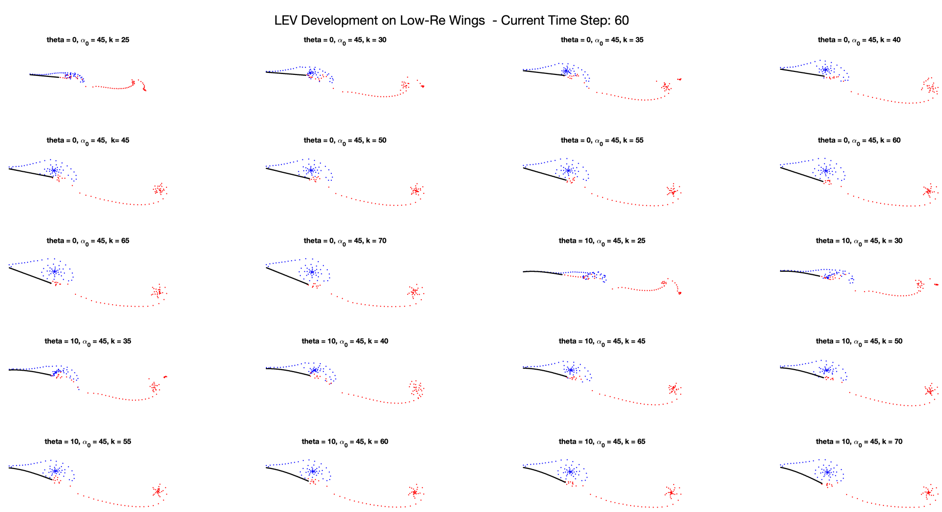

Figure 25. Lift and Drag Coefficient evolution with respect to time-step, with initial incidence angle of 45 degrees and different spring constants, $t^* = 5.12$.

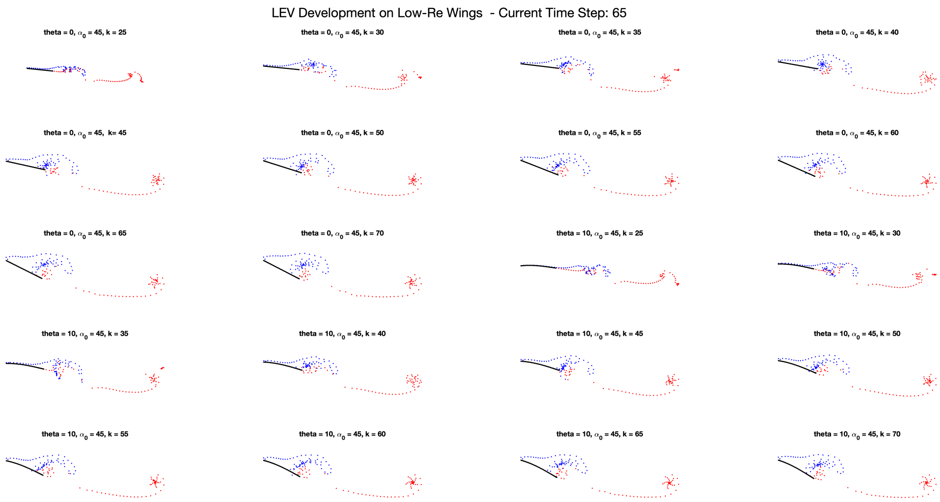

Figure 26. Lift and Drag Coefficient evolution with respect to time-step, with initial incidence angle of 45 degrees and different spring constants, $t^* = 5.54$.

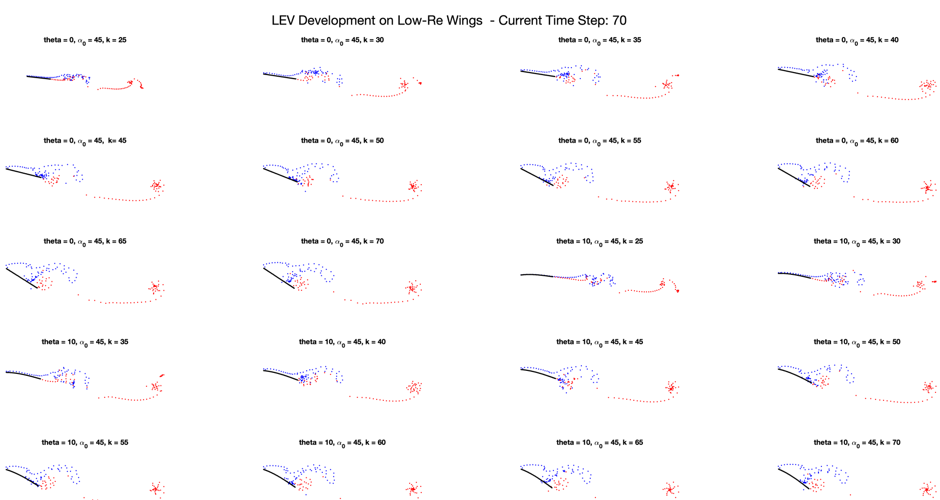

Figure 27. Lift and Drag Coefficient evolution with respect to time-step, with initial incidence angle of 45 degrees and different spring constants, $t^* = 5.97$.